Comparison of discrete transfer and Monte-Carlo methods for radiative heat transfer in three-dimensional non-homogeneous scattering media

Henson, J.C. and Malalasekera, W., Numerical Heat Transfer Part A: Applications, 32(1), July 1997, pp 19-36, ISSN 1040-7782.

COMPARISON OF THE DISCRETE TRANSFER AND MONTE CARLO METHODS FOR RADIATIVE HEAT TRANSFER IN THREE-DIMENSIONAL, NONHOMOGENEOUS, SCATTERING MEDIA

J. C. Henson and W. M. G. Malalasekera

Department of Mechanical Engineering, Loughborough University,

Loughborough, Leicestershire LE11 3TU, United Kingdom.

ABSTRACT

Modified formulations of the discrete transfer and Monte Carlo methods are presented for the prediction of radiative heat transfer in three-dimensional, nonhomogeneous, participating media. Numerical solutions found with both algorithms are in good agreement with published benchmark results which used contemporary methods to determine the radiative transport in a unit cube. New solutions in an arbitrary L-shaped geometry using a nonorthogonal, body-fitted mesh are also presented. The average deviation between the two methods is less than 1.2% for both the boundary surface flux and the divergence of radiative flux or gas emissive power within the enclosed, isotropically scattering media.

NOMENCLATURE

A_i	area of subsurface *i*, m^2
E_g	gas blackbody emissive power, W/m^2
E_s	surface blackbody emissive power, W/m^2
G	incident radiation, W/m^2
$\overline{G_iG_j}$	volume-to-volume total exchange area, m^2
$\overline{G_iS_j}$	volume-to-surface total exchange area, m^2
I	intensity of radiation, W/m^2 sr

I_b	blackbody intensity, W/m^2 sr
$\hat{\mathbf{n}}$	normal unit vector to a surface
q_-	incident heat flux onto a surface, W/m^2
q_+	emitted heat flux from a surface, W/m^2
$\mathbf{q}$	heat flux vector, W/m^2
Q_g	net radiative heat source in a volume, W
Q_s	net radiative heat flow on a surface, W
$\dot{Q}'''$	heat production per unit volume, W/m^3
R	random number from uniform distribution
s	mean scattering path length, m
δs	path length interval, m
s_n	best estimate of standard deviation
$\hat{\mathbf{s}}$	unit vector in a given direction
S	radiative source function, W/m^2 sr
S_n	best estimate of standard error
$\overline{S_i G_j}$	surface-to-volume total exchange area, m^2
$\overline{S_i S_j}$	surface-to-surface total exchange area, m^2
V_i	volume of subvolume i, m^3
x	simulation result for a radiative quantity
$\bar{x}$	mean; best estimate of true solution value
x, y, z	Cartesian coordinates, m

Greek Symbols

β	extinction coefficient, 1/m
ε	emissivity
κ	absorption coefficient, 1/m
ξ, η, γ	coordinates in local mapping coordinate system
ϕ_{ij}	reception factor between two elements *i* and *j*
σ	scattering coefficient, 1/m
ψ_n	bilinear shape functions
ω	single scattering albedo
Ω	solid angle, sr

INTRODUCTION

The calculation of radiative heat transfer demands a numerical technique flexible enough to deal with the complex geometries and the nonhomogeneous radiative properties that often arise in practical situations. For example, in fire and combustion systems a non-uniform distribution of temperature and absorbing gaseous species concentrations is often present, together with fluid flow and other modes of heat transfer. In these combined mode problems, it is advantageous if the radiative heat transfer equation can be solved over the same non-orthogonal curvilinear meshes as are typically employed by most modern Computational Fluid Dynamics (CFD) solvers. Finally, any numerical technique must be computationally efficient so as to minimise run-times and storage requirements.

Unfortunately, there is no existing method which has been able to satisfy all these criteria and establish itself as a clear ‘winner’. Several of the more popular techniques include the zonal method (Hottel and Cohen [1]), the Monte Carlo method (Howell [2]; Modest [3]; Farmer [4]), the discrete transfer method (Lockwood and Shah [5]), the spherical harmonics (P-N) method (Mengüç and Viskanta [6]), the discrete ordinates (S-N) method (Fiveland [7]), the finite element method

(Razzaque *et al.* [8]) , the finite volume method (Raithby and Chui [9]) and the YIX method (Tan and Howell [10]). All have been successfully used to predict radiative heat transfer in both multi-dimensional rectangular and cylindrical geometries, and practical applications where the topology can be fitted into a cylindrical or Cartesian geometrical framework. However, numerical calculations with more complex geometries are comparatively rare. Historically, the inherent flexibility of the Monte Carlo method that arises from its ray tracing basis has favoured its use with complex geometries [11], not possible with contemporary techniques. Furthermore, recognising its ability to provide an exact solution within a statistical uncertainty, it is ideal for validating other numerical methods [12]. Recently, Chai *et al.* [13] used a 'cell blocking' procedure to approximate inclined and curved boundaries with a stepped Cartesian outline suitable for a discrete ordinates solution. While, Fiveland and Jessee [14] have proposed an alternative finite element formulation of the discrete ordinates method suitable for multidimensional problems with irregular shaped boundaries. Chui and Raithby [15] demonstrated the ability of the finite volume method to calculate radiative heat transfer in two-dimensional irregular geometries, which in principle, can be extended to three-dimensional arbitrary geometries.

The discrete transfer method, a hybrid of the Monte Carlo, zonal and discrete ordinates methods, is particularly suited to complex geometries, since it combines the ray tracing basis of the former stochastic method with the faster deterministic nature of the later two methods. Murthy and Choudhury [16] and Meng *et al.* [17] have both presented discrete transfer calculations on two-dimensional irregular grids, the later study using an unstructured triangular mesh. In addition, cases with isotropically scattering media were considered, with verification against previous discrete transfer solutions by Carvalho *et al.* [18] and other numerical methods on a regular Cartesian grid. Haidekker *et al.* [19] compared Monte Carlo and discrete transfer solutions for absorbing and emitting media contained within three-dimensional arbitrary geometries discretised with curvilinear grids. Further cases have been presented by Malalasekera and James [20] with validation against

exact solutions and other methods. However, there appears to be no reported calculations using the discrete transfer method in three-dimensional, scattering media.

This paper therefore focuses on examining the applicability of the discrete transfer method to radiative heat transfer in scattering media, particularly in nonorthogonal geometries. Detailed numerical solutions for a three-dimensional L-shaped geometry containing an absorbing, emitting and isotropically scattering media are presented. This geometry, previously studied by Malalasekera and James [20] is particularly interesting because of its body-fitted mesh together with the shadowing effects that arise from the bend, and is further enhanced by considering a nonhomogeneous extinction coefficient. Comparisons are made with calculations from a hybrid zonal/Monte Carlo code to ensure a valid set of numerical solutions, and both numerical methods are first verified against solutions by Hsu and Farmer [21] and Burns *et al.* [22] for an orthogonal cubic geometry.

GOVERNING EQUATIONS AND SOLUTION PROCEDURE

Detailed descriptions of the discrete transfer and Monte Carlo methods can be found in Lockwood and Shah [5] and Farmer and Howell [23, 24] respectively, so only aspects of the algorithms relevant to the issues addressed in this paper are considered. With both methods the geometry is discretised into control volumes. For complex geometries this involves fitting a curvilinear coordinate system to the boundary such that the surface mesh description incorporates all the geometrical detail. Both methods are then built on a ray tracing concept, but differences arise from the nature in which the ray directions are chosen and the quantities evaluated along their path.

The Discrete Transfer Method

The discrete transfer method solves for the intensity distribution along representative rays between two boundary surfaces with the recurrence relation:

$$I_{n+1} = I_n e^{-\delta s^*} + S(1 - e^{-\delta s^*}) \tag{1}$$

where *n* and *n*+1 designate successive cell boundary locations, separated by a distance $\delta s = \delta s^* / \beta$, as the ray passes through each control volume. The source function, *S*, and the extinction coefficient, β, are both assumed constant over the interval, δs. In the solution procedure, rays are emitted from the centre of each boundary subsurface, P, in directions determined by discretising the 2π hemispherical solid angle above the surface into *N* finite solid angles, $\delta\Omega$. Eq. (1) is then applied in the direction QP (see Fig. 1) along each ray, and summing the radiative heat flux contributions for each solid angle gives the incident flux for the subsurface. i.e.

$$q_- = \sum_{j=1}^{N} I(\hat{\mathbf{s}}_j)(\hat{\mathbf{n}} \cdot \hat{\mathbf{s}}_j)\delta\Omega_j \tag{2}$$

An initial intensity value $I_o = q_+ / \pi$ is used for each subsurface, where the emitted flux, q_+ is given by:

$$q_+ = (1-\varepsilon)q_- + \varepsilon E_s \tag{3}$$

Since q_+ depends on the value of q_-, an iterative solution is required, unless the surfaces are black. The net radiative heat flow for each subsurface, area A, is then:

$$Q_s = A(q_+ - q_-) \tag{4}$$

Solution of Eq. (1) also requires a value for the source function *S*, where with isotropic in-scattering:

$$S = (1-\omega)I_b + \frac{\omega}{4\pi}\int_{4\pi} I(\hat{\mathbf{s}}_i)d\Omega_i \tag{5}$$

When the single scattering albedo, ω is equal to zero, the source expression simplifies to the blackbody intensity, I_b. However, for a non-zero albedo, augmentation due to in-scattering along $\hat{\mathbf{s}}_i$ occurs and this incident radiation, *G*, is discretised as:

$$G = \int_{4\pi} I(\hat{\mathbf{s}}_i)d\Omega_i \cong \frac{4\pi\sum \bar{I}(\hat{\mathbf{s}}_i)\delta\Omega_i}{\sum \delta\Omega_i} \tag{6}$$

where $\bar{I}$ is the arithmetic mean of the entering and leaving radiant intensities of each ray passing through the subvolume within the finite solid angle $\delta\Omega_i$. In contrast with the previous implementations (e.g. Meng *et al.* [17]), the summation is weighted by the solid angle, since this gives a more conservative approximation for *G*.

The divergence of the radiative heat flux, $\nabla \cdot \mathbf{q}$ is presumed constant in each subvolume and can be determined directly from the gas blackbody intensity, I_b, and incident radiation function, G, as:

$$\nabla \cdot \mathbf{q} = \kappa(4\pi I_b - G) \tag{7}$$

This term is used in the energy transport equation to couple the radiative heat transfer with other transport phenomena. The net radiative heat source within each subvolume is then:

$$Q_g = (\nabla \cdot \mathbf{q})\delta V \tag{8}$$

where δV is the element volume. Alternatively, Lockwood and Shah [5] evaluated the total source in a subvolume by summing the energy contribution from each ray passing through it, but for the calculations in this paper, the approach in Eqs. (6)–(8) was found to give slightly better predictions.

For a uniform heat generation, $\dot{Q}'''$ in each subvolume, $\nabla \cdot \mathbf{q}$ is replaced by $\dot{Q}'''$ in Eq. (7) and substitution into (5) gives the radiative source function for an isotropically scattering medium as:

$$S = \frac{1}{4\pi}\left[\frac{\dot{Q}'''}{\beta} + G\right] \tag{9}$$

Finally, note that an iterative solution is required with both scattering and source prescribed problems due to the dependence of the source function on G.

The Monte Carlo Method

A Monte Carlo ray tracing method is used to simulate radiative heat transfer by randomly releasing a statistically large number of energy bundles and tracking their progress through the participating medium. Several algorithms have been proposed as described by Farmer [4] and this implementation uses a computationally efficient version with essentially three distinguishing features:

(i) The power content of a bundle is partitioned into the subvolumes along its path such that the absorbed fraction in any volume is:

$$\text{Absorbed fraction} = 1 - e^{-\kappa \delta s} \tag{10}$$

where δs is the path length in each subvolume with homogeneous absorption coefficient, κ.

(ii) The probable distance a bundle travels before a scattering collision is determined from a cumulative distribution function. A random number R is selected from a uniform distribution between 0 and 1 to determine the scattering path length as:

$$s = -\frac{1}{\sigma} \ln R \tag{11}$$

In nonhomogeneous media the scattering coefficient, σ varies along the bundle path, although usually its value is presumed constant over each subvolume. A summation is then taken for each subvolume, n, through which the bundle travels such that a scattering collision only occurs when:

$$\sum_n \sigma_n \delta s_n > -\ln R \tag{12}$$

(iii) The absorption calculation in Eq. (10) is only performed as a bundle exits a subvolume. When multiple scattering events occur within a single subvolume, the path length is accumulated, rather than evaluating the expensive exponential term after each collision, resulting in a significant speed-up.

Other aspects of this pathlength-based algorithm, such as modelling the bundles' emission and scattering behaviour, are identical to the traditional collision-based Monte Carlo method and can be found in [3, 25]. However, as this study is concerned with applying the Monte Carlo technique to nonorthogonal geometries, special treatment is required to select the bundle emission points within the irregular subsurfaces and subvolumes that arise from the curvilinear coordinate system. A finite element parametric mapping technique is used to map points selected in a square or cubic master element to the corresponding irregular subregions in the physical geometry. First, random numbers (ξ, η, γ) are chosen for each coordinate direction from a uniform distribution and these are then used to derive bilinear shape functions, $\psi_n(\xi, \eta, \gamma)$ appropriate for the master element shape. The emission location (x, y, z) is then interpolated from either the surface or volume nodal coordinates (x_n, y_n, z_n) using the expression:

$$x = \sum_n x_n \psi_n(\xi, \eta, \gamma) \tag{13}$$

where the other two coordinates are found by replacing *x* in Eq. (13) by *y* or *z*. Furthermore, the initial energy of each bundle must be adjusted to counter the effects of the nonuniform mapping and ensure the correct distribution of radiant energy over the area or volume of the physical element. This adjustment is made by weighting the bundle energy by the determinant of the Jacobian of the transformation calculated for each starting location.

Since the convergence and accuracy of the Monte Carlo method depends on the randomness of its sampling technique, this implementation uses a recent random number generator algorithm by Marsaglia [26] which can rapidly produce random 32 bit sequences with a very large periods (i.e. 2^{250}).

As bundles are traced through the geometry, the total exchange areas between the surface and volume elements are automatically determined as follows:

Surface-to-surface: $\overline{S_i S_j} = A_i \varepsilon_i \phi_{ij}$

Surface-to-volume: $\overline{S_i G_j} = A_i \varepsilon_i \phi_{ij}$

Volume-to-surface: $\overline{G_i S_j} = 4_i \kappa_i V_i \phi_{ij}$

Volume-to-volume: $\overline{G_i G_j} = 4_i \kappa_i V_i \phi_{ij}$ (14)

where ϕ_{ij} is the fraction of the total energy released by element *i*, that is absorbed by element *j*, both directly and indirectly after scattering interactions along the bundle paths and reflection at the surface elements. Therefore if the surface and gas black body emissive powers are denoted by E_s and E_g respectively, a radiative energy balance for each of the *N* subsurfaces is given by:

$$Q_{si} = \varepsilon_i A_i E_{si} - \sum_{j=1}^{N} \overline{S_i S_j} E_{sj} - \sum_{k=1}^{K} \overline{S_i G_k} E_{gk} \qquad i = 1,2,\ldots N \tag{15}$$

where Q_{si} is the net radiative heat flow on the surface with area A_i and emissivity ε_i. Similarly, an energy balance for each of the *K* subvolumes, gives the net radiative heat source, Q_{gi} as:

$$Q_{gi} = 4\kappa_i V_i E_{gi} - \sum_{j=1}^{N} \overline{G_i S_j} E_{sj} - \sum_{k=1}^{K} \overline{G_i G_k} E_{gk} \qquad i = 1,2,\ldots K \tag{16}$$

Therefore, the net heat source in each subvolume can be determined directly for a known gas emissive power. However, for an applied source condition, the resulting system of equations must be solved using an iteration scheme, matrix inversion or some other matrix solution technique, to determine the gas emissive powers. The present method employs a successive-over-relaxation (SOR) iterative solver [27] to speed-up computation, particularly when the exchange area matrices are large.

It is noteworthy that after the total exchange areas have been determined by Monte Carlo simulation, they can be used repeatedly to quickly calculate new radiative heat transfer solutions for various temperature or heat source conditions, depending on the problem type. The optical properties (i.e. gas extinction coefficient, surface emissivity) must be temperature-independent, and therefore probably gray as well, but there are no restrictions on the optical thickness or isotropy of scattering with this hybrid Monte Carlo/zonal method [4]. A new Monte Carlo simulation is then only required when the geometry or optical properties are modified.

The Ray Tracing Algorithm

The major computational effort in both the discrete transfer and Monte Carlo methods is spent tracing the ray or bundle paths through the mesh subvolumes in the discretised radiation space. Since only the path length information is required by both formulations a common algorithm is used in the coding of both methods. Optimisation of this algorithm is essential to maximise the overall efficiency of each method. Furthermore, ray tracing through a curvilinear mesh requires a robust approach able to handle any distortion in the subvolumes or precision problems [28] that can arise from floating-point errors, particularly when edge intersections occur. The first difficulty can be overcome by representing all non-planar faces as triangles, such that each face of a hexahedral element is considered as two triangles. A review of several ray-polygon intersection techniques found that an algorithm by Bodouel [29] is extremely fast for finding ray-*triangle* intersections.

Essentially Bodouel determines the intersection point in terms of the triangle's barycentric coordinates (α, β) as shown in Fig. 2.

As an added advantage, in the authors' implementation of this algorithm these coordinates are also used to detect edge intersections (i.e. $\alpha \approx 0$, $\beta \approx 0$). In this event, the intersection point is moved infinitesimally away from the edge to avoid floating-point imprecision and speed-up the search procedure for the next intersection. Finally, it should be noted that this ray tracing algorithm would be equally effective for geometries meshed with tetrahedral elements and in unstructured arrangements after appropriate modification of the indexing procedure.

RESULTS AND DISCUSSION

An assessment of the error in the Monte Carlo and discrete transfer numerical results must be available before a useful comparison can be made. With insufficient spatial and angular discretisation of the radiation space, inaccuracies can arise with the discrete transfer method from so-called 'ray-effects', while the statistical scatter between Monte Carlo simulations can become unacceptably large. Conversely, excessive run-times will result if the discretisation is made too fine. For the problems analysed below, 400 solid angle divisions per subsurface have been used with the discrete transfer method. Prior investigations found this was sufficient to give solution values within 1% of their converged value, achieved only with very fine discretisation (i.e. 1600+ solid angle divisions) for the mesh sizes used.

An advantage of the Monte Carlo method is that, since it is a sampling technique, its solution accuracy can be estimated statistically. Several independent simulations must be conducted, each with a unique set of random numbers. Then, if each of these n simulations gives an estimated result, x, for a radiative quantity (i.e. surface heat flux, divergence of radiative flux or gas emissive power), the best estimate of the true solution value is their arithmetic mean, $\bar{x}$. The accuracy of this estimate, and hence the solution accuracy, is called the standard error. Applying the central limit theorem, the estimated standard error, S_n, is given by Barford [30] as:

$$S_n(\bar{x}) = \frac{s_n(x)}{\sqrt{n}} = \frac{1}{\sqrt{n(n-1)}} \sqrt{\sum_i (x_i - \bar{x})^2} \tag{17}$$

where s_n is the best estimate for the standard deviation of the sample distribution of *x*. It is found that S_n decreases only as $1/\sqrt{n}$ (for large values of *n*), so the computational effort is often better spent improving the intrinsic accuracy of each sample result *x*, embodied in the quantity s_n, by using a larger number of energy bundles per simulation. Furthermore it is important to use these bundles efficiently by releasing more in regions with a higher radiative emission. Hence, in the current Monte Carlo algorithm the number of energy bundles released in a subvolume is directly proportional to the absorption coefficient and emissive power within the volume. Table 1 shows the total number of energy bundles and number of simulations used for the problems considered. In each case, the best estimate of the standard error has been calculated and is quoted with the solution values in Tables 2, 3 and 5. This enables confidence limits to be determined for each Monte Carlo result. For example, with 68% confidence the true solution value lies within the limits $\bar{x} \pm S_n$, or with 99% confidence within $\bar{x} \pm 2.58 S_n$. The run-times and average relative differences between values from the Monte Carlo and discrete transfer solutions are also summarised in Table 1 for each problem. Since both methods are executed on a HP-9000/750 machine, with identical compiler options, these run-times should be directly comparable. Note that the run-times increase for the discrete transfer method when the scattering albedo is non-zero since several iterations are required to establish the incident radiation, *G*, from in-scattering as defined in Eq. (6). Conversely, Monte Carlo run-times decrease with increased albedo because the scattering tends to spread out the bundle paths improving the uniformity of emission. Therefore less bundles per simulation are required to achieve comparable intrinsic accuracy. Finally, note that in the problems considered all the calculated surface heat fluxes are negative, but to simplify the presentation only positive values are shown.

Case 1: Verification Against Benchmark Solutions

Numerical solutions employing the Monte Carlo and YIX methods [21], together with subsequent finite element comparisons [22], are used to verify the present Monte Carlo and discrete transfer formulations. The problem geometry is a unit cube enclosing an isothermal, absorbing, emitting and isotropically scattering medium. All the surfaces of the enclosure are cold and black so there is no emission or reflection from the boundaries. Radiative properties in the medium are influenced by a shaped optical thickness for which the extinction coefficient varies according to the relation:

$$\beta(x,y,z) = 0.9\left(1-2|x|\right)\left(1-2|y|\right)\left(1-2|z|\right)+0.1 \qquad \text{[1/m]} \tag{18}$$

where the coordinate origin lies at the cube centre and $-0.5 \le (x,y,z) \le 0.5$ is the domain of computation. Assuming unity blackbody emissive power in the medium, results are sought for a single scattering albedo of $\omega = 0$ (i.e. pure absorption) and $\omega = 0.9$.

To obtain solutions with the present methods, the geometry is discretised with a 9×9×9 orthogonal mesh of cubic subvolumes each with a side length of 1/9. The volume centres are then located symmetrically about the principal coordinate axes at $(x,y,z) = (0, \pm 1/9, \pm 2/9, \pm 3/9, \pm 4/9)$. At each position the extinction coefficient is evaluated from Eq. (18) and presumed constant over the surrounding subvolume.

Tables 2 and 3 summarise the results determined with the present methods together with published solutions [21, 22] for the boundary surface flux and divergence of radiative flux in the medium respectively. Both tables show results for pure absorption and a single scattering albedo of $\omega = 0.9$. When comparing the solutions it should be noted that in contrast to the other methods, the finite element formulation allows for the variation in radiative properties across each subvolume. Therefore, for verification purposes a fair comparison is only reasonable between the other four methods which all assume homogeneous elements, although the finite element results have been included in acknowledgement that they represent a slightly more accurate solution. Examination of

the tables clearly show that the results from the present formulations are in excellent agreement with the YIX and Monte Carlo results provided by Hsu and Farmer [21]. The maximum deviation between all four methods is less than 2.2% for both the flux divergence and surface flux values (where the relative difference of each value was determined with respect to the finite element value).

A solution was also determined with the discrete transfer method for a 27×27×27 mesh to verify that with greater spatial discretisation the formulation is able to capture more of the variation in radiative properties and more closely match the finite element solution. Table 4 shows a comparison of the new discrete transfer solution with corresponding finite element and YIX solutions [22] for the pure absorption problem. As anticipated, the deviation between the 9×9×9 finite element results and the 27×27×27 discrete transfer results for the surface heat flux is now under 0.70% of the finite element result compared to 2.55% previously. This improvement is comparable to the closer agreement achieved with the 27×27×27 YIX method. Finally, to take full advantage of the better spatial discretisation with the discrete transfer method, a finer angular discretisation should be used. A solution with 1600 solid angle deviations per subsurface further reduced the maximum deviation with the finite element result to under 0.51%.

Case 2: L-shaped Geometry Enclosing An Isothermal, Participating Medium

The problem geometry is discretised with a 20×7×7 body-fitted mesh of hexahedral elements as shown in Fig. 3. All the surfaces are black with an emissive power, $E_s = 0.25$ and enclose an isothermal, absorbing, emitting and isotropically scattering medium with unity blackbody emissive power. An arbitrary optical thickness distribution has been chosen such that most of the radiation is emitted from a dense region centred on the corner diagonal away from the boundaries. The variation in extinction coefficient is given by the expressions:

$$x \le -y: \quad \beta = 0.9(1.5+x)\left(1-2|y|\right)(1-2|z|)\Big/\left(1.5-y\right)+0.1 \qquad \text{[1/m]}$$

$$x > -y: \quad \beta = 0.9(1-2|x|)\left(2.5-y\right)(1-2|z|)\Big/(2.5+x)+0.1 \qquad \text{[1/m]} \qquad (19)$$

Sample surface heat flux values calculated along the two lines A-A and B-B (see Fig. 3) are given in Table 5. Results have been determined for both purely absorbing and isotropically scattering ($\omega = 0.9$) media, and the corresponding contours for the divergence of radiative flux at $z = 0$ are shown in Figs. 4a and 4b respectively. These plots clearly reveal the strong influence from the variation in extinction coefficient, with a high radiative source from the optically thick central region which then gradually decreases towards the boundaries. Only one set of contour plots are reproduced from both methods, since the differences between the divergence values are indistinguishable when displayed graphically. This is not surprising, as the average deviation between each pair of divergence solutions is only 1.15% and 0.13% for the pure absorption and scattering problems respectively (see Table 1).

Case 3: L-shaped Geometry Enclosing A Participating Medium With A Volumetric Heat Source

The problem geometry and variation in extinction coefficient is identical to that specified in Case 2. However, now all surfaces are cold and black and a volumetric heat source is prescribed in the medium so the variation in gas emissive power and radiative surface flux is sought. Considering the L-shaped as two volumes separated along the corner diagonal (i.e. at $x = -y$), heat sources $\dot{Q}_1'''$ and $\dot{Q}_2'''$ are specified in the smaller and larger volumes respectively. Results have been determined for a uniform source in the entire medium ($\dot{Q}_1''' = \dot{Q}_2''' = 1$) and for a discontinuous source across the corner diagonal ($\dot{Q}_1''' = 1,\ \dot{Q}_2''' = 0.5$). In both problems a single scattering albedo of $\omega = 0.5$ was arbitrary chosen, although only the gas emissive powers are effected by this choice, since the surface heat fluxes are independent of the scattering albedo for isotropically scattering media. Table 5 presents sample surface heat flux values along the two lines A-A and B-B (see Fig. 3) from both solutions. The average deviation between the Monte Carlo and discrete transfer flux values is slightly higher for the discontinuous source problem at 1.14% as compared with a deviation of 1.11% with the uniformly distributed heat source. The gas emissive power contours at $z = 0$ are also

plotted for each problem in Figs. 5a and 5b. The shape of the contours for the problem with a uniform heat source (Fig. 5a) closely resemble those in Case 2 for the variation of the divergence of radiative flux in an isothermal medium. Clearly this arises from the strong influence of the nonhomogeneous extinction coefficient such that a colder dense central region is surrounded by hotter gas near the boundaries. A similar variation in temperature is observed in the medium with the non-uniform volumetric source (Fig. 5b). However, the contours are now strongly asymmetric, particularly in the central region, as a result of the abrupt discontinuity in source values across the corner diagonal. A numerical comparison of all the gas emissive power values calculated by both methods showed an average deviation of only 0.5% for both problems.

CONCLUDING REMARKS

Formulations for both the discrete transfer and pathlength-based Monte Carlo methods have been presented for three-dimensional radiative transport in nonhomogeneous participating media. Results from these formulations are in good agreement with previously published data using the YIX and Monte Carlo methods. However, finer discretisation or appropriate modifications are required to match slightly more accurate solutions achieved with the finite element method which accounts for the variation of radiative properties in a subvolume. Farmer [4] has proposed schemes for the Monte Carlo method to accommodate nonhomogeneous volume elements in both emissive power and attenuation, but clearly longer run-times result from the additional calculations. A new set of numerical solutions has been calculated for a three-dimensional L-shaped geometry enclosing isotropically scattering, nonhomogeneous media. In the four problems considered, the average deviation between each pair of solutions from the Monte Carlo and discrete transfer methods is less than 1.2% and as low as 0.13%. This comparison is based on values for both the surface heat flux and the divergence of radiative flux or gas emissive power within the temperature or source prescribed media.

The speed and simplicity of the discrete transfer method favours its selection for radiative heat transfer calculations in the large complex geometries that often arise in fire and combustion systems. However, a principal limitation of the discrete transfer formulation is its restriction to problems involving diffusely reflecting boundaries and isotropically scattering media. As the problem complexity increases the inherent flexibility and power of the Monte Carlo method tends to compensate for its large computational requirement. In principle, exact simulation of all important physical processes is possible, including the radiative behaviour of real surfaces and Mie scattering. As a final point, the performance of both the discrete transfer and Monte Carlo methods can be expected to significantly improve with the new generation of massively parallel machines to which their ray tracing methodology is easily adapted.

ACKNOWLEDGEMENTS

The authors would like to thank Professor John R. Howell (The University of Texas at Austin), Dr. Jeff T. Farmer (NASA Marshall Space Flight Center) and Dr. Shawn P. Burns (Sandia National Laboratories) for their helpful discussions and information.

REFERENCES

1. H. C. Hottel and E. S. Cohen, Radiant Heat Exchange in a Gas-Filled Enclosure: Allowance for Nonuniformity of Gas Temperature, *AIChE J.*, vol. 4, pp. 3-14, 1958.
2. J. R. Howell, Application of Monte Carlo to Heat Transfer Problems, in T. I. Irvine and J. P. Harnett (eds.), *Advances in Heat Transfer*, vol. 5, pp. 1-54, Academic Press, New York, 1968.
3. M. F. Modest, *Radiative Heat Transfer*, chap. 19, McGraw Hill, New York, 1993.
4. J. T. Farmer, Improved Algorithms for Monte Carlo Analysis of Radiative Heat Transfer in Complex Participating Media, Ph.D. dissertation, The University of Texas at Austin, 1995.

5. F. C. Lockwood and N. G. Shah, A New Radiation Solution Method for Incorporation in General Combustion Prediction Procedures, in *Eighteenth Symposium (International) on Combustion*, pp. 1405-1414, The Combustion Institute, 1981.
6. M. P. Mengüç and R. Viskanta, Radiative Transfer in Three-Dimensional Rectangular Enclosures Containing Inhomogeneous, Anisotropically Scattering Media, *J. Quant. Spectrosc. Radiat. Transfer*, vol. 33, no. 6, pp. 533-549, 1985.
7. W. A. Fiveland, Three-Dimensional Radiative Heat Transfer Solutions by the Discrete-Ordinates Method, *AIAA J. Thermophys. Heat Transfer*, vol. 2, no. 4, 1988, pp. 309-316, 1988.
8. M. M. Razzaque, J. R. Howell, and D. E. Klein, Coupled Radiative and Conductive Heat Transfer in a Two-Dimensional Rectangular Enclosure with Gray Participating Media Using Finite Elements, in Y. Mori and W. Yang (eds.*), ASME, JSME Thermal Engineering Joint Conference Proceedings*, pp. 41-48, 1983.
9. G. D. Raithby and E. H. Chui, A Finite-Volume Method for Predicting Radiant Heat Transfer in Enclosures with Participating Media, *ASME J. Heat Transfer*, vol. 112, pp. 415-423, 1990.
10. Z. Tan and J. R. Howell, New Numerical Method for Radiation Heat Transfer in Nonhomogeneous Participating Media, *AIAA J. Thermophys. Heat Transfer*, vol. 4, no. 4, pp. 419-424, 1990.
11. P. V. Villeneuve, D. Chapman, and J. R. Mahan, Use of the Monte-Carlo Ray-Trace Method as a Design Tool for Jet Engine Infrared Visibility Suppression, in *Radiative Heat Transfer: Current Research*, ASME HTD-vol. 276, pp. 59-71, 1994.
12. G. Parthasarathy, H. S. Lee, J. C. Chai, and S. V. Patankar, Monte Carlo Solutions for Radiative Heat Transfer in Irregular Two-Dimensional Geometries, *ASME J. Heat Transfer*, vol. 117, pp. 792-794, 1995.
13. J. C. Chai, H. S. Lee, and S. V. Patankar, Treatment of Irregular Geometries using a Cartesian-Coordinates-Based Discrete-Ordinates Method, in *Radiative Heat Transfer – Theory and Applications*, ASME HTD-vol. 244, pp. 49-54, 1993.

14. W. A. Fiveland and J. P. Jessee, A Finite Element Formulation of the Discrete-Ordinates Method for Multidimensional Geometries, in *Radiative Heat Transfer – Theory and Applications*, ASME HTD-vol. 244, pp. 41-48, 1993.
15. E. H. Chui, and G. D. Raithby, Computation of Radiant Heat Transfer on a Nonorthogonal Mesh using the Finite-Volume Method, *Numer. Heat Transfer, Part B Fundam.*, vol. 23, pp. 269-288, 1993.
16. J. Y. Murthy and D. Choudhury, Computation of Participating Radiation in Complex Geometries, in *Developments in Radiative Heat Transfer*, ASME HTD-vol. 203, pp. 153-160, 1992.
17. F. L. Meng, F. McKenty, and R. Camarero, Radiative Heat Transfer by the Discrete Transfer Method using an Unstructured Mesh, in *Radiative Heat Transfer – Theory and Applications*, ASME HTD-vol. 244, pp. 55-66, 1993.
18. M. G. Carvalho, T. Farias, and P. Fontes, Predicting Radiative Heat Transfer In Absorbing, Emitting, And Scattering Media Using The Discrete Transfer Method, in *Fundamentals of Radiation Heat Transfer*, ASME HTD-vol. 160, pp. 17-26, 1991.
19. A. Haidekker, A. Charette, and Y. S. Kocaefe, Application of the Hybrid Zone/Monte Carlo Method to 3-D Curvilinear Grids in Radiative Heat Transfer, *Int. J. Numer. Meth. Eng.*, vol. 37, pp. 203-216, 1994.
20. W. M. G. Malalasekera and E. H. James, Calculation of Radiative Heat Transfer in Three-Dimensional Complex Geometries, in *Proc. 30th 1995 National Heat Transfer Conf. Vol. 13*, ASME HTD-vol. 315, pp. 53-61, 1995.
21. P. Hsu and J. T. Farmer, Benchmark Solutions of Radiative Heat Transfer within Nonhomogeneous Participating Media using the Monte Carlo and YIX Methods, in *Proc. 30th 1995 National Heat Transfer Conf. Vol. 13*, ASME HTD-vol. 315, pp. 29-36, 1995.

22. S. P. Burns, J. R. Howell, and D. E. Klein, Finite Element Solution for Radiative Heat Transfer with Nongray, Nonhomogeneous Radiative Properties, in *Proc. 30th 1995 National Heat Transfer Conf. Vol. 13*, ASME HTD-vol. 315, pp. 3-10, 1995.
23. J. T. Farmer and J. R. Howell, Hybrid Monte Carlo/Diffusion Methods For Enhanced Solution Of Radiative Transfer In Optically Thick Nongray Media, in *Radiative Heat Transfer: Current Research*, ASME HTD-vol. 276, pp. 203-212, 1994.
24. J. T. Farmer and J. R. Howell, Monte Carlo Prediction of Radiative Heat Transfer in Inhomogeneous, Anisotropic, Nongray Media, *AIAA J. Thermophys. Heat Transfer*, vol. 8, no. 1, pp. 133-139, 1994.
25. R. Siegel and J. R. Howell, *Thermal Radiation Heat Transfer*, 3rd ed., pp. 795-800, Hemisphere, Washington, 1992.
26. G. Marsaglia, G., Department of Statistics, Florida State University, e-mail: geo@stat.fsu.edu (Posted on internet newsgroup: sci.math.num-analysis), 1994.
27. C. Hirsch, *Numerical Computation of Internal and External Flows. Vol. 1: Fundamentals of Numerical Discretization*, pp. 471-473, John Wiley & Sons, Chichester, 1988.
28. E. Haines, Essential Ray Tracing Algorithms, in A. S. Glassner (ed.), *An Introduction To Ray Tracing*, pp. 46-47, Academic Press, New York, 1989.
29. D. Badouel, An Efficient Ray-Polygon Intersection, in A. S. Glassner (ed.), *Graphics Gems*, pp. 390-393, Academic Press, New York, 1990.
30. N. C. Barford, *Experimental Measurements: Precision, Error and Truth*, 2nd ed., chaps. 2 & 6, John Wiley & Sons, Chichester, 1985.

Table 1 Comparison of CPU run-times and average relative differences for each problem, together with the number of simulations and total number of energy bundles used in each Monte Carlo solution.

CASE	Scattering albedo, ω	DT CPU[a] time [s]	MC CPU[a] time [s]	MC no. of simulations	MC total no.[b] of bundles	ARD[c] of Q_s/A_s [%]	ARD[c] of $\nabla\cdot\mathbf{q}$ or E_g [%]
C1.1	0.0	50	24621	30	$9.954\cdot10^7$	0.64	0.66
C1.2	0.9	245	2943	30	$1.062\cdot10^7$	0.51	0.08
C2.1	0.0	66	25300	10	$9.746\cdot10^7$	0.96	1.15
C2.2	0.9	460	2492	10	$8.663\cdot10^6$	1.04	0.13
C3.1	0.5	520	22965	10	$8.605\cdot10^7$	1.11	0.47
C3.2	0.5	520	22960	10	$8.605\cdot10^7$	1.14	0.50

[a]CPU run-times on HP-9000/750.

[b]MC total number of energy bundles = bundles/simulation × number of simulations.

[c]Average relative difference: $\mathrm{ARD} = 1/n\sum\left|(\mathrm{DT}-\mathrm{MC})/\mathrm{MC}\right|$ for n values (i.e. N surfaces fluxes or K volumetric quantities).

Table 2 Surface heat fluxes at (-0.5,0,*z*) for case C1.

CASE	C1.1 ($\omega = 0$)					C1.2 ($\omega = 0.9$)				
z	**MC**	**DT(400)**	MC[d]	YIX[d]	FE[e]	**MC**	**DT(400)**	MC[d]	YIX[d]	FE[e]
±4/9	**0.10857**	**0.10967**	0.10959	0.10872	0.10743	**0.01213**	**0.01217**	0.01219	0.01214	0.01193
±3/9	**0.14012**	**0.14107**	0.14125	0.14171	0.13759	**0.01573**	**0.01574**	0.01564	0.01589	0.01536
±2/9	**0.16566**	**0.16645**	0.16729	0.16619	0.16255	**0.01867**	**0.01870**	0.01892	0.01877	0.01826
±1/9	**0.18468**	**0.18543**	0.18552	0.18569	0.18049	**0.02104**	**0.02094**	0.02103	0.02107	0.02037
0	**0.19239**	**0.19286**	0.19260	0.19291	0.18760	**0.02176**	**0.02182**	0.02202	0.02192	0.02120
	MC: S_n < 0.00050 (all values on surface)					MC: S_n < 0.00008 (all values on surface)				

[d]Hsu and Farmer [21].

[e]Burns *et al.* [22].

Table 3 Divergence of the radiative heat fluxes at (x,0,0) for case C1.

CASE	C1.1 ($\omega = 0$)					C1.2 ($\omega = 0.9$)				
x	**MC**	**DT(400)**	MC[d]	YIX[d]	FE[e]	**MC**	**DT(400)**	MC[d]	YIX[d]	FE[e]
±4/9	**0.72336**	**0.72860**	0.72910	0.72219	0.72502	**0.07914**	**0.07921**	0.07974	0.07912	0.07916
±3/9	**1.37701**	**1.38099**	1.38739	1.37209	1.38007	**0.15748**	**0.15751**	0.15866	0.15739	0.15750
±2/9	**1.96893**	**1.96458**	1.98360	1.95658	1.97318	**0.23496**	**0.23495**	0.23673	0.23482	0.23506
±1/9	**2.51700**	**2.52182**	2.53635	2.49628	2.52438	**0.31191**	**0.31202**	0.31433	0.31163	0.31205
0	**3.07462**	**3.08144**	3.09813	3.03664	3.08571	**0.38894**	**0.38911**	0.39192	0.38842	0.38916
	MC: S_n < 0.00035 (all values on plane)					MC: S_n < 0.00001 (all values on plane)				

[d]Hsu and Farmer [21].

[e]Burns *et al.* [22].

Table 4 Surface heat fluxes at (-0.5,0,*z*) for problem C1.1 with YIX and discrete transfer methods for finer spatial discretisation.

C1.1 (ω = 0)				
z	FE[e]	YIX[e]	**DT(400)**	**DT(1600)**
	(9×9×9)	(27×27×27)		
±4/9	0.10743	0.10718	**0.10808**	**0.10798**
		(-0.23%)[f]	**(0.61%)**	**(0.51%)**
±3/9	0.13759	0.14032	**0.13809**	**0.13821**
		(1.98%)	**(0.36%)**	**(0.45%)**
±2/9	0.16255	0.16388	**0.16361**	**0.16327**
		(0.82%)	**(0.65%)**	**(0.44%)**
±1/9	0.18049	0.18248	**0.18176**	**0.18136**
		(1.10%)	**(0.70%)**	**(0.48%)**
0	0.18760	0.18946	**0.18868**	**0.18848**
		(0.99%)	**(0.58%)**	**(0.47%)**

[e]Burns *et al.* [22].

[f]Deviation of value as % of FE value.

Table 5 Surface heat fluxes at (-1.5,y_1,0) & (-0.5,y_2,0) for cases C2 and C3.

	Case 2: Temperature prescribed problem.				Case 3: Source prescribed problem.			
	C2.1 ($\omega = 0$)		C2.2 ($\omega = 0.9$)		C3.1 ($\dot{Q}_1''' = \dot{Q}_2''' = 1$)		C3.2 ($\dot{Q}_1''' = 1, \dot{Q}_2''' = 0.5$)	
y_1	MC	DT(400)	MC	DT(400)	MC	DT(400)	MC	DT(400)
-3/7	0.08767	0.08919	0.00996	0.01001	0.19044	0.19040	0.18368	0.18298
-2/7	0.10655	0.10705	0.01199	0.01201	0.22396	0.22387	0.21637	0.21650
-1/7	0.11905	0.12011	0.01354	0.01351	0.23962	0.24105	0.23138	0.23312
0	0.12440	0.12474	0.01404	0.01406	0.24413	0.24227	0.23492	0.23453
1/7	0.12096	0.12147	0.01384	0.01370	0.23808	0.23930	0.22913	0.23153
2/7	0.10796	0.10911	0.01198	0.01230	0.22157	0.22109	0.21329	0.21388
3/7	0.08847	0.08976	0.00987	0.01014	0.18610	0.18561	0.17754	0.17886
y_2								
7/12	0.19715	0.19587	0.02408	0.02419	0.26617	0.26751	0.14914	0.14891
9/12	0.18887	0.18880	0.02262	0.02292	0.26676	0.26858	0.14118	0.14321
11/12	0.17963	0.17987	0.02120	0.02166	0.26562	0.26926	0.13819	0.14047
13/12	0.17069	0.17247	0.01976	0.02031	0.26463	0.26852	0.13610	0.13830
15/12	0.16006	0.16138	0.01866	0.01888	0.26423	0.26627	0.13404	0.13580
17/12	0.15028	0.15003	0.01732	0.01742	0.26107	0.26318	0.13252	0.13334
19/12	0.13790	0.13890	0.01573	0.01592	0.25737	0.25909	0.13019	0.13069
21/12	0.12656	0.12568	0.01423	0.01440	0.25217	0.25389	0.12665	0.12773
23/12	0.11389	0.11424	0.01269	0.01280	0.24442	0.24506	0.12290	0.12309
25/12	0.10035	0.10092	0.01100	0.01114	0.23191	0.23227	0.11627	0.11656
27/12	0.08476	0.08475	0.00940	0.00932	0.21039	0.21104	0.10632	0.10585
29/12	0.06537	0.06571	0.00719	0.00714	0.17129	0.17249	0.08637	0.08650
	MC: $S_n < 0.00085$		MC: $S_n < 0.00020$		MC: $S_n < 0.00095$		MC: $S_n < 0.00060$	

Figure Captions

Figure 1 A representative geometry with ray traces from a subsurface P through the mesh.

Figure 2 Parametric representation of the ray intersection point P with the barycentric coordinates α and β.

Figure 3 L-shaped geometry for cases C2 and C3 discretised using a body-fitted mesh (20×7×7) geometry with uniform interpolation along each boundary and the coordinate origin positioned at the centre of the corner diagonal. All dimensions are in metres. The calculated surface heat flux values along A–A and B–B are tabulated in Table 5.

Figure 4 L-shaped problem radiative flux divergence contours at (x, y, 0) for: (a) Case C2.1 (pure absorption); (b) Case C2.2 ($\omega = 0.9$).

Figure 5 L-shaped problem gas emissive power contours at (x, y, 0) for: (a) Case C3.1 (uniform heat source); (b) Case C3.2 (non-uniform heat source).

OR use 4-figure group with following caption and modify references in text (page 16, 2 places) from Fig. 5a and Fig. 5b to Fig. 4c and Fig. 4d respectively.

Figure 4 L-shaped problem solution contours at (x, y, 0) for: (a) radiative flux divergence in case C2.1 (pure absorption); (b) radiative flux divergence in case C2.2 (ω = 0.9); (c) gas emissive power in case C3.1 (uniform heat source); (d) gas emissive power in case C3.2 (non-uniform heat source).

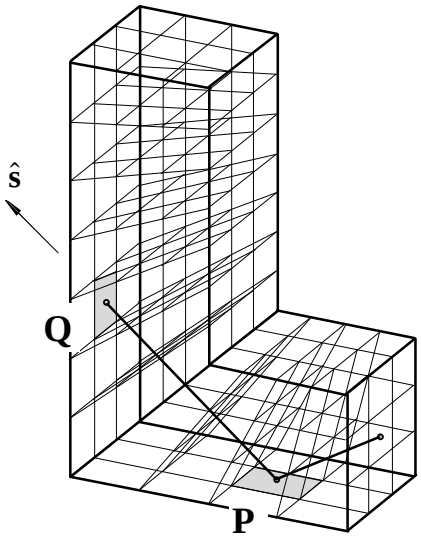

Figure 1

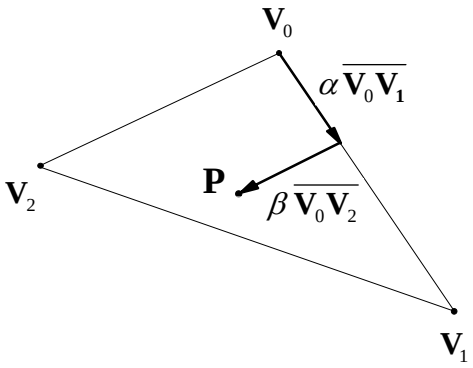
$\mathbf{V}_0$
$\alpha\,\overline{\mathbf{V}_0\mathbf{V}_1}$
$\mathbf{P}$
$\beta\,\overline{\mathbf{V}_0\mathbf{V}_2}$
$\mathbf{V}_2$
$\mathbf{V}_1$

Figure 2

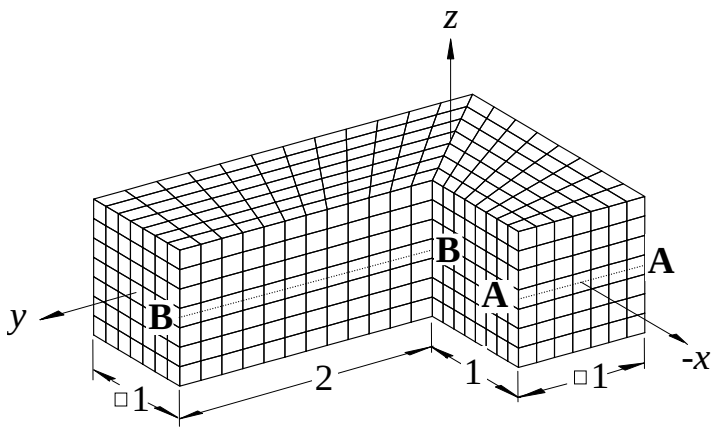

Figure 3

(a)

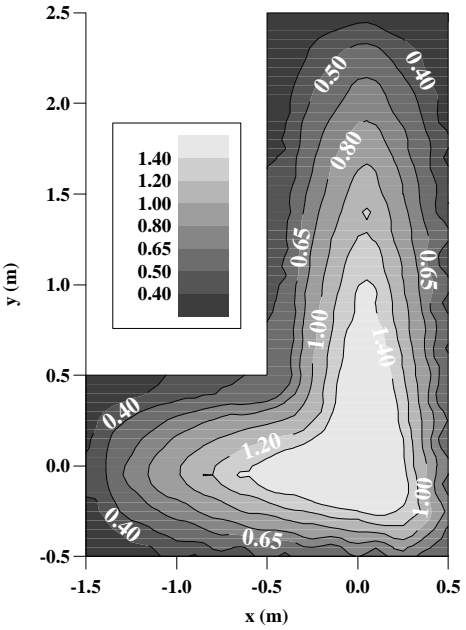
1.40
1.20
1.00
0.80
0.65
0.50
0.40
y (m)
x (m)
2.5
2.0
1.5
1.0
0.5
0.0
-0.5
-1.5
-1.0
-0.5
0.0
0.5

(b)

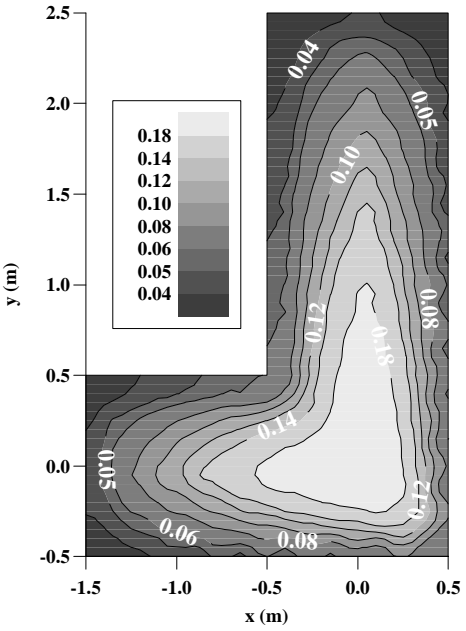
0.18
0.14
0.12
0.10
0.08
0.06
0.05
0.04
y (m)
x (m)
2.5
2.0
1.5
1.0
0.5
0.0
-0.5
-1.5
-1.0
-0.5
0.0
0.5

Figure 4

(a)

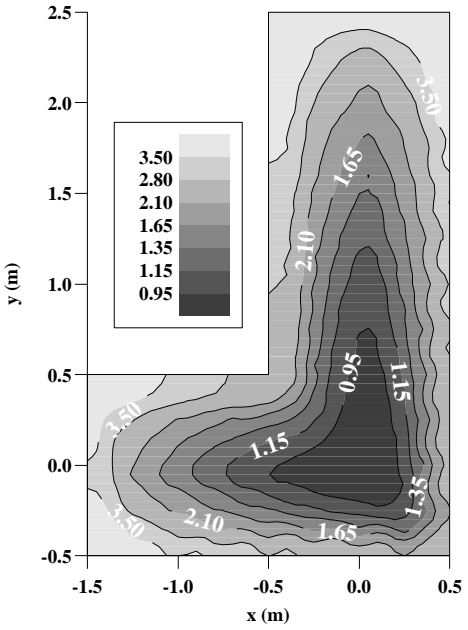
3.50
2.80
2.10
1.65
1.35
1.15
0.95
y (m)
x (m)
2.5
2.0
1.5
1.0
0.5
0.0
-0.5
-1.5
-1.0
-0.5
0.0
0.5

(b)

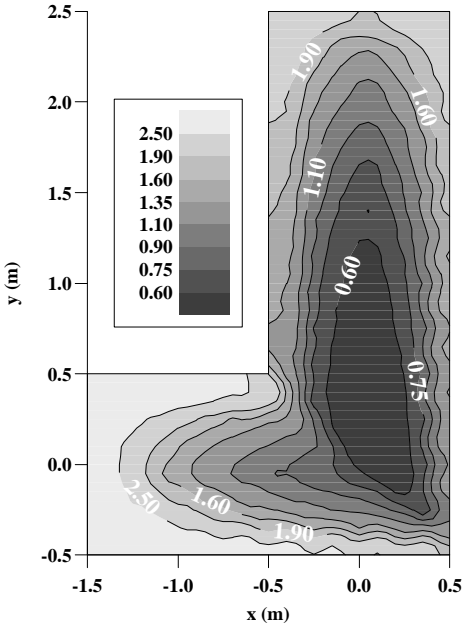
2.50
1.90
1.60
1.35
1.10
0.90
0.75
0.60
y (m)
x (m)
2.5
2.0
1.5
1.0
0.5
0.0
-0.5
-1.5
-1.0
-0.5
0.0
0.5

Figure 5

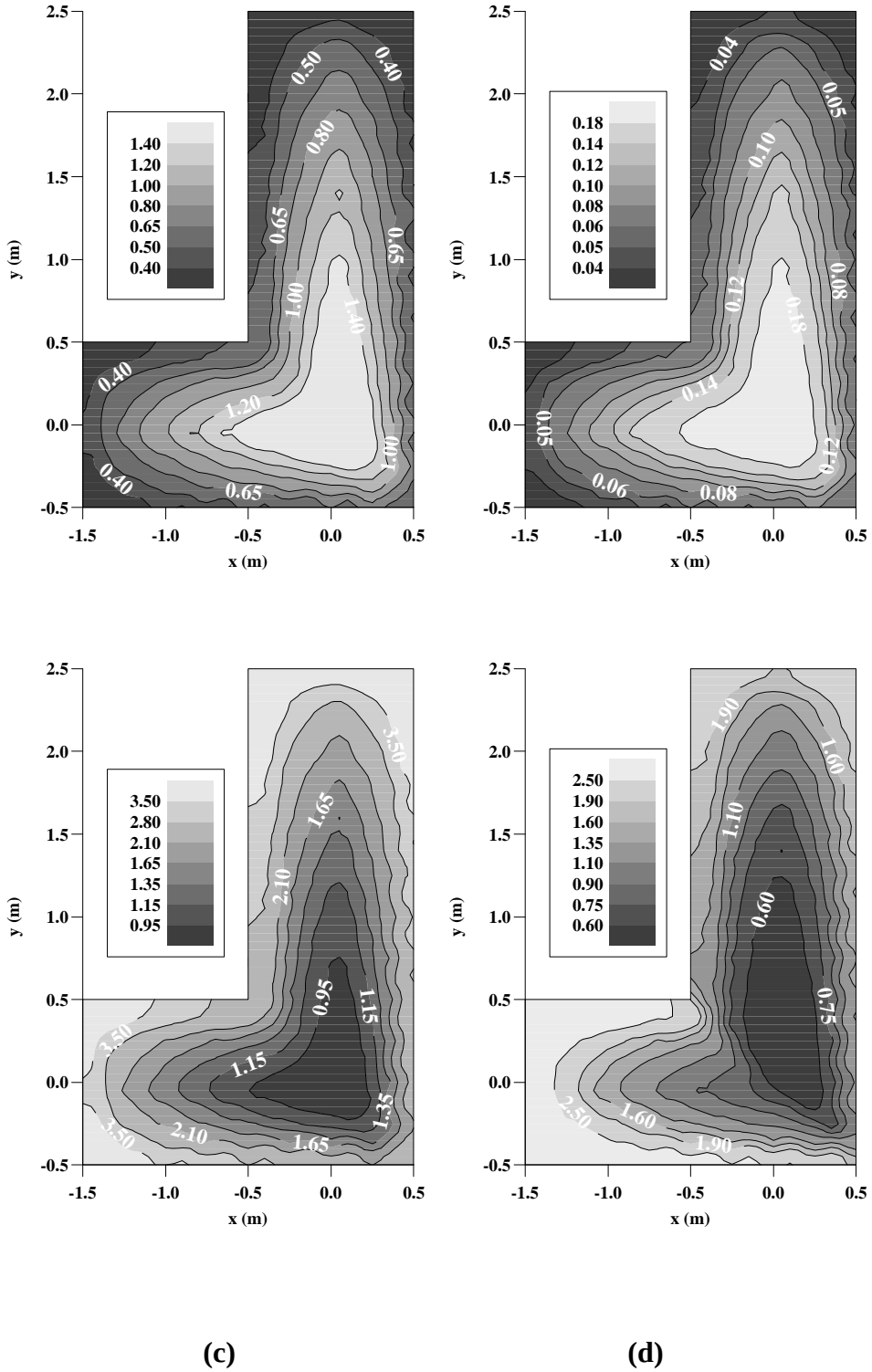

Figure 4
(Alternative to separate Figure 4 and Figure 5 – see captions page)